

LARGE SCALE ANALYSIS OF THE VON KÁRMÁN SODIUM EXPERIMENT USING PROPER ORTHOGONAL DECOMPOSITION

V. Botez, R. Bousquet, C. Nore

Laboratoire Interdisciplinaire des Sciences du Numérique, CNRS, Campus universitaire Paris-Saclay, rue du Belvédère, 91400 Orsay, France

In 2006, the von Kármán sodium (VKS) experiment was able to produce a dynamo effect using liquid sodium driven by two counter-rotating impellers in a cylindrical cavity. We analyze simulations of this setup both in growth and saturated dynamo regimes using the Proper Orthogonal Decomposition (POD). In the growth phase, the magnetic field generated is essentially an axial dipole supplemented with secondary structures which are shown to be emerging from the α -effect. The most surprising result is found in the saturated phase, where the magnetic field feedback breaks the symmetry of the velocity field even though it is in an exactly counter-rotating configuration.

Introduction.

Magnetic fields are omnipresent in the universe so that their study is crucial for understanding the large-scale structures at stake, the interaction between celestial bodies but also the apparition of life on the Earth. It is well-known, for instance, that the Earth's magnetic field has undergone several reversals over time, with a seemingly random duration between each one. The solar magnetic field, on the contrary, is oscillatory with a fixed period of approximately 22 years. A number of models have attempted to study the mechanisms behind reversals, but we are still struggling to understand the mechanisms behind those occurring on the Earth. Different attempts at reproducing the phenomenon behind all these magnetic fields were successfully conducted: the Riga experiment based on the Ponomarenko dynamo [1], the Karlsruhe experiment based on the Roberts dynamo [2], both in the late 1990's, and the von Kármán Sodium (VKS) experiment in Cadarache, France, conducted from the 2000's to 2010's. The last one is particular in that until now it is the only successful experiment without a constrained flow and based on its highly turbulent state.

The aim of this paper is to perform a numerical analysis of the large-scale structures emerging from a configuration which successfully produced dynamo instabilities during the VKS experiments.

1. Governing equations and numerical setup.

In the general incompressible setup, without external forcing and in their dimensionless form, the magnetohydrodynamics (MHD) equations read as follows:

$$\frac{\partial \mathbf{u}}{\partial t} + (\mathbf{u} \cdot \nabla) \mathbf{u} = -\nabla P + \frac{1}{\text{Re}} \nabla^2 \mathbf{u} + \mathbf{J} \times \mathbf{B}, \quad \nabla \cdot \mathbf{u} = 0, \quad (1)$$

and

$$\frac{\partial \mathbf{B}}{\partial t} = \nabla \times (\mathbf{u} \times \mathbf{B}) - \frac{1}{\text{Rm}} \nabla \times \left(\frac{1}{\sigma_r} \nabla \times \left(\frac{\mathbf{B}}{\mu_r} \right) \right), \quad \nabla \cdot \mathbf{B} = 0, \quad (2)$$

with \mathbf{u} being the velocity field, P the pressure, \mathbf{B} the magnetic induction field, \mathbf{J} the electric current density, μ_r and σ_r accounting for the space and time variation of the

magnetic permeability and electrical conductivity and defined through $\mu = \mu_0\mu_r$ and $\sigma = \sigma_0\sigma_r$ (with μ_0 being the vacuum magnetic permeability and σ_0 the sodium electrical conductivity), and, finally, $\text{Re} = \omega R_{\text{cyl}}^2/\nu$ and $\text{Rm} = \omega R_{\text{cyl}}^2\mu_0\sigma_0$ being the kinetic and the magnetic Reynolds number, respectively, defined by the rotation frequency ω of the impellers and by the radius R_{cyl} of the cylinder. Equations (1)–(2) are simulated using cylindrical coordinates with the code SFEMaNS (for Spectral/Finite Element code for Maxwell and Navier–Stokes equations) which is an in-house massively parallelized code. It decomposes the azimuthal direction into Fourier modes and uses finite elements in the meridional planes [3]. The von Kármán setup modelled here has an aspect ratio, height over cylinder radius, $H/R_{\text{cyl}} = 2$, uses two unscooping exactly counter-rotating impellers fitted with 8 blades (called TM73) as in the actual experiment [4], and has an exterior copper wall. The setup is denoted as **R** in Fig. 6 in [5]. These impellers are modelled by means of a pseudo-penalty technique [6]. Most importantly, the impellers are made of soft iron with high relative magnetic permeability, modelled by $\mu_r = 50$ in our simulations. Indeed the presence of soft iron somewhere in the rotating impellers has proved to be an essential experimental asset [5] to have a low enough threshold Rm^c for the system to exhibit dynamo. The role of this material was also considered in kinematic dynamo simulations [7, 8]. The high value of μ_r has in fact been shown to lower the dynamo threshold to a point where it could be reached by experiments in [9].

In this specific setup, simulations are parallelized on 64 Fourier modes and 3 meridional sections which contain in total around 60000 nodes, therefore, requiring 192 CPUs. We use a time-step $dt = 0.00125$. An MHD simulation is initialized with an already statistically stationary velocity field and a low magnitude magnetic field with random seed. Following [10], we will consider the configuration $(\text{Re}, \text{Rm}) = (1500, 150)$ which is indeed above the dynamo threshold in the configuration used [9].

2. Basics of proper orthogonal decomposition (POD).

Applied on statistically stationary fields, POD [11] allows separation of variables of a time and space dependent field $f(t, x)$ on modes which are orthonormal with respect to the usual Euclidean norm. It reads:

$$f(t, x) = \sum_n a_{n,t} \phi_{x,n}, \quad (3)$$

$$\langle \phi_{\cdot,n} | \phi_{\cdot,m} \rangle = \delta_{n,m},$$

with $\phi_{x,n}$ being the POD modes, $a_{n,t}$ their time-amplitude, and $\delta_{n,m}$ the Kronecker symbol. Then the amplitudes $a_{n,t}$ being uncorrelated, we find that their mean value over a specific time-window T , $\langle a_{n,t} a_{m,t} \rangle_T = \delta_{n,m} \lambda_n$ can be interpreted as the energy of the n -th POD mode among the total energy $\langle \int_{\Omega} f^2 \rangle_T = \sum_n \lambda_n$. Finally, rearranging the labels n in the decreasing order of mean energy allows us to find the dominant structures in terms of energy. In this paper we use the method of snapshots [12] with a sampling time $\delta t = 1$ to preserve us from any stroboscopic effect related to the impellers' period of rotation $\Delta t = 2\pi$. As explained in [13], it is possible to augment the data by applying the symmetry of the system to our snapshots. In the exactly counter-rotating configuration, the geometry is R_π -symmetric [14], i.e. it is invariant under a rotation of π over a horizontal axis going through the cylinder's center. In addition, considering the TM73 impellers with 8 blades, the geometry is invariant under the rotations $\theta \rightarrow \theta + k2\pi/8$ for any integer k which we write S_k . In the following, we consider R_π -symmetry and invariance under S_4 .

Introducing these symmetries within our snapshots forces the POD modes to be either symmetric or antisymmetric with respect to the specific R_π -symmetry. On the one hand, we expect the mean component of the flow to be dominantly axisymmetric and R_π -symmetric, as shown in [15]. On the other hand, the introduction of the S_4 symmetry will make it possible to separate the even and odd Fourier modes (m_F), which is useful for separating the axisymmetric $m_F = 0$ modes and the $m_F = 3$ modes resulting from the Kelvin–Helmholtz instability [9, 14].

As the magnetic energy reads $E_m = \frac{1}{2} \mathbf{B} \cdot \mathbf{H}$ with $\mathbf{B} = \mu_0 \mu_r \mathbf{H}$, so that $\mathbf{B} \neq \mathbf{H}$ within the impellers, applying POD to \mathbf{B} or \mathbf{H} gives mathematically different results. Since we are more interested in the bulk dynamics rather than in that of the impellers, we choose to apply POD to \mathbf{H} rather than to \mathbf{B} . In the following, ϕ_n and ψ_n label the n -th POD modes of \mathbf{u} and \mathbf{H} , respectively, and their associated time-amplitudes are a_n and b_n .

3. Application of POD to \mathbf{u} and \mathbf{H} in the growth phase.

In this section, we apply POD to the velocity field and magnetic field during the growth phase. Because in this regime the magnetic field is exponentially growing, we cannot apply POD directly as later times \mathbf{H} snapshots would bias the statistics. So, in this section, each snapshot of \mathbf{H} is normalized by its L_2 norm to get rid of this exponential growth, and this new field is denoted as \mathbf{H}_N . In the following, $\psi_{N,n}$ is the n -th POD mode of \mathbf{H}_N . As the flow is fluctuating, the magnetic field cannot be strictly written as $\mathbf{H}(t, \mathbf{x}) = e^{\lambda t} \mathbf{H}_p(\mathbf{x})$, but would be better described by $\mathbf{H}(t, \mathbf{x}) = e^{\lambda t + \eta(t)} \mathbf{H}_N(t, \mathbf{x})$ with \mathbf{H}_N of norm 1 and η a time-dependent fluctuation such that $\langle \eta(t) \rangle_T = 0$. Therefore, studying \mathbf{H}_N allows us to investigate the time fluctuations of the dominant eigenmode.

The results displayed in the following are computed using 400 snapshots from the growth phase to which are added their S_4 rotated samples. Then we apply R_π -symmetry and get a total of 1600 snapshots. Fig. 1 shows the POD spectra of \mathbf{u} and \mathbf{H}_N . Fig. 2 shows the Fourier spectra of a few POD modes obtained by computing the amplitudes of the Fourier components and multiplying them by the average energy contained within each POD mode. We give a brief explanation of the results on \mathbf{u} following the more detailed analysis of [15]. The ϕ_0 mode (76.1% of \mathbf{u} 's energy) is R_π -symmetric (Fig. 1a), dominated by its axisymmetric component (Fig. 2a) and with the amplitude oscillating around a non-zero mean value (Fig. 3a). It is, therefore, the mode containing the velocity's mean-field. In the 2D representation of its axisymmetric component (Fig. 4a), we can recognize the two cells driven by the counter-rotating impellers [16]. Next ϕ_1 and ϕ_2

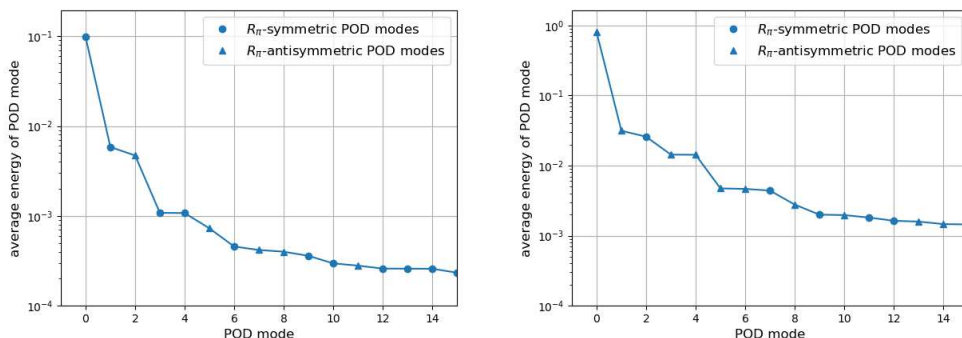


Fig. 1. POD spectra (average energies in the time window studied) in the growth phase at $Re = 1500$, $Rm = 150$, $\mu_r = 50$. (a) POD spectrum of \mathbf{u} . (b) POD spectrum of \mathbf{H}_N .

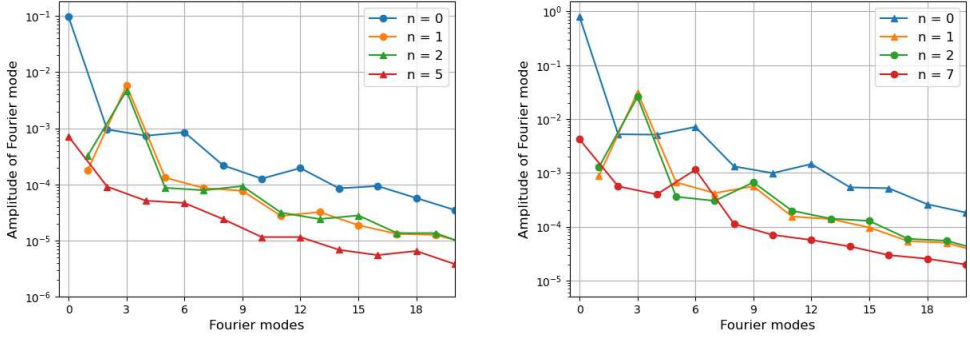


Fig. 2. Fourier spectra of the main POD modes in the growth phase at $\text{Re} = 1500$, $\text{Rm} = 150$, $\mu_r = 50$. Note that the spectra have either odd or even Fourier modes but never couple the two. Modes with circles (resp. triangles) are R_π -symmetric (resp. R_π -antisymmetric). (a) POD modes of \mathbf{u} . (b) POD modes of \mathbf{H}_N .

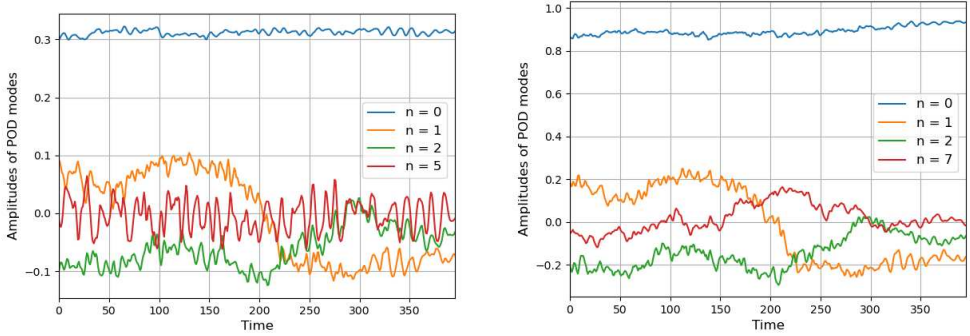


Fig. 3. Time evolution of the main POD modes in the growth phase (only the time window without data-augmentation is displayed). (a) POD modes of \mathbf{u} . (b) POD modes of \mathbf{H}_N .

(gathering 8.2% of \mathbf{u} 's energy) are dominated by $m_F = 3$ (Fig. 2a). As explained in [15], these modes are associated with the Kelvin–Helmholtz instability occurring around the shear layer at $z = 0$ [14]. Since this major instability of the von Kármán flow is due to an odd Fourier mode, it justifies our choice to separate the Fourier components $m_F = 0$ and $m_F = 3$ by introducing the S_4 symmetry. Their common structures (Figs. 6 and 10 in [15]), opposite symmetries (Fig. 1a) and amplitudes in quadrature (Fig. 3a) can be interpreted as a rotation in time of the Kelvin–Helmholtz rolls. To continue, $\boldsymbol{\phi}_3$ and $\boldsymbol{\phi}_4$ (1.7% of \mathbf{u} 's energy, not shown) are dominated by their $m_F = 8$ component and are highly localized within the 8 blades. It can be shown, assuming as observed that their time-amplitudes are quadratic cosines and sines, that their common structures and individual symmetries sum up to waves propagating clockwise in the upper half of the cylinder and anti-clockwise in the lower half when looking from above, as expected for unscoping counter-rotating impellers. Eventually, $\boldsymbol{\phi}_5$ (0.57% of \mathbf{u} 's energy) is R_π -antisymmetric, dominated by its axisymmetric component (Fig. 2a) and shows a time-amplitude oscillating around 0. The axisymmetric component of this mode, illustrated in Fig. 4b, consists of a large cell that occupies the entire volume. It is this component which breaks the

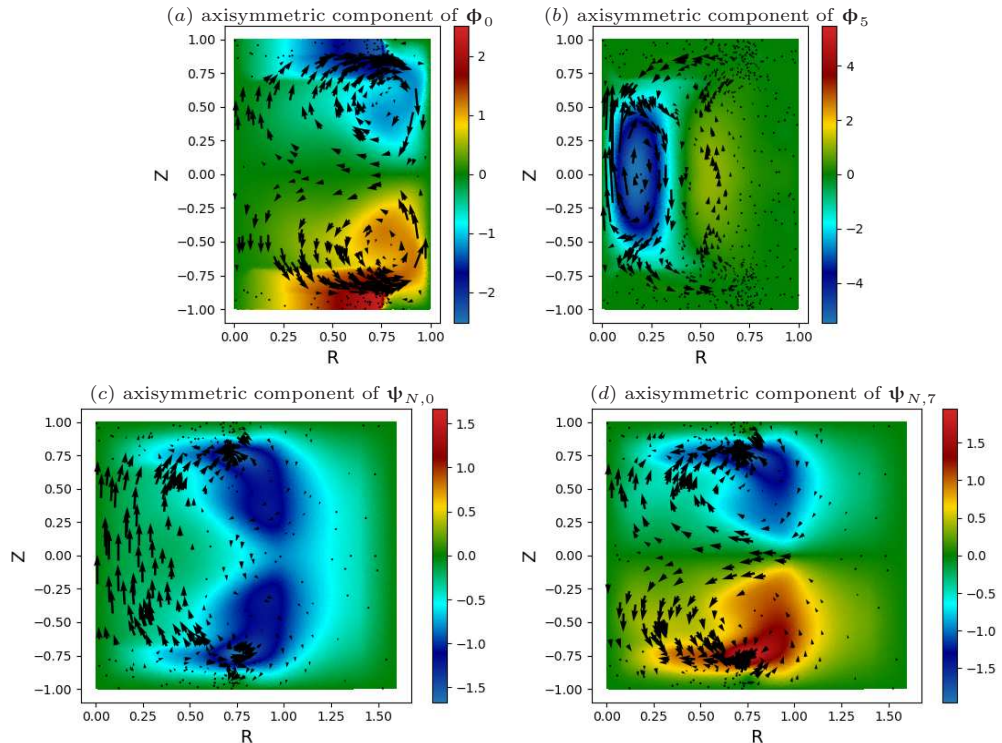


Fig. 4. 2D representation of the main axisymmetric POD modes in the growth phase. Panels (a) and (b) (resp., (c) and (d)) have opposite symmetries and are the mean axisymmetric components of \mathbf{u} (resp. \mathbf{H}_N). Colors represent the amplitude of the azimuthal component, and 2D-vectors are composed of the radial and axial components. In the time window studied, Φ_5 and $\Psi_{N,7}$ have time-amplitudes oscillating around 0.

R_π -symmetry of the flow studied in [17] and which contains most of the flow's angular momentum [15]. Put altogether, these modes represent 86.6% of \mathbf{u} 's energy.

We now perform the same analysis on \mathbf{H}_N . The mode $\Psi_{N,0}$ (79.9% of \mathbf{H}_N 's energy) is R_π -antisymmetric (Fig. 1b), dominated by its axisymmetric component (Fig. 2b) and with the amplitude oscillating around a non-zero mean value (Fig. 3b). It is the mode containing the growing axial dipole of the dominant eigenmode [9, 18]. Then $\Psi_{N,1}$ and $\Psi_{N,2}$ (5.7% of \mathbf{H}_N 's energy) are dominated by $m_F = 3$ (Fig. 2b). Here the analysis regarding quadratures, symmetries and, therefore, rotations is the same as above for \mathbf{u} . Interestingly, Fig. 3 suggests that these two modes give rise to a rotation which is synchronized with the Kelvin–Helmholtz rolls observed in \mathbf{u} . It can be explained by adapting the idea of POD Galerkin [19] as follows: in the ideal case, where the growing magnetic field's time-derivative is dominated by the exponential growth with growth-rate λ , the induction equation can be rewritten as

$$\lambda \mathbf{B}_N = \nabla \times (\mathbf{u} \times \mathbf{B}_N) - \frac{1}{\text{Rm}} \nabla \times \left(\frac{1}{\sigma_r} \nabla \times \left(\frac{\mathbf{B}_N}{\mu_r} \right) \right)$$

with $\mathbf{B}_N \simeq \mathbf{H}_N$ within the bulk. Then projecting onto the $\Psi_{N,n}$ and neglecting the

Ohmic dissipation, we find $b_i \propto \sum_{j,k} b_j a_k K_{ijk}$. The tensor

$$K_{ijk} = \langle \boldsymbol{\psi}_{N,i} | \nabla \times (\boldsymbol{\phi}_k \times \boldsymbol{\psi}_{N,j}) \rangle$$

can be interpreted as the energy sent from $\boldsymbol{\phi}_k$ to $\boldsymbol{\psi}_{N,i}$ mediated by $\boldsymbol{\psi}_{N,j}$. Contrary to the usual POD Galerkin, the relations given by projections are equalities between the time-amplitudes and not ODEs. In the case $i = 1$ (resp. $i = 2$), the numerical calculations show that the dominant contributions arise from K_{101} (resp. K_{202}): in other words, $\boldsymbol{\phi}_1$ (resp. $\boldsymbol{\phi}_2$) gives energy to $\boldsymbol{\psi}_{N,1}$ (resp. $\boldsymbol{\psi}_{N,2}$) by interacting with the growing axial dipole $\boldsymbol{\psi}_{N,0}$. This is not surprising since we expect a highly helical velocity field around $z = 0$ due to the Kelvin–Helmholtz vortices and, therefore, an α -effect with the opposite sign to the one occurring at z near the blades [20]. This amounts to the conversion of a poloidal component $\boldsymbol{\psi}_{N,0}$ into mainly toroidal components $\boldsymbol{\psi}_{N,1}$ and $\boldsymbol{\psi}_{N,2}$.

Then $\boldsymbol{\psi}_{N,3}$, $\boldsymbol{\psi}_{N,4}$, $\boldsymbol{\psi}_{N,5}$ and $\boldsymbol{\psi}_{N,6}$ (3.8% of \mathbf{H}_N 's energy, not shown in Figs 2b and 3b) are dominated for the first two by their $m_F = 8$ component and the last two by their $m_F = 16$ component. They account for the time and space variation of μ_r within the impellers and are analogous to those encountered in \mathbf{u} . Eventually, $\boldsymbol{\psi}_{N,7}$ (0.4% of \mathbf{H}_N 's energy) is R_π -symmetric, dominated by its axisymmetric component (Fig. 2b), and shows a time-amplitude oscillating around 0. This mode is, in analogy with $\boldsymbol{\phi}_5$ for \mathbf{u} , a symmetry-breaking mode of the dominant component of the eigenmode. We found from Galerkin projections that this mode emerges from the interaction between the dominant axisymmetric modes of \mathbf{u} and \mathbf{H}_N , but also from the interactions of all POD modes carrying $m_F = 3$ Fourier components. As shown in Fig. 4d, its axisymmetric component displays a cell in each half of the domain with opposite rotations, pointing to a dominant quadrupole. In general, these modes represent 89.8% of the energy of the growing eigenmode.

4. Application of POD to \mathbf{u} and \mathbf{H} in the saturated phase.

In this section we apply POD to the velocity field and to the magnetic field during the saturated phase. The results are computed using 600 snapshots from the saturated phase, to which are added their S_4 -rotated samples. Then we apply R_π -symmetry and get a total of 2400 snapshots. As seen in Fig. 5, \mathbf{u} and \mathbf{H} are dominated by, respectively, an R_π -symmetric and an R_π -antisymmetric POD mode. The mode $\boldsymbol{\phi}_0$ gathers 78.5% of \mathbf{u} 's energy and $\boldsymbol{\psi}_0$ 86.65% of \mathbf{H} 's energy. According to Fig. 6, these modes are dominated by their axisymmetric components. Their spatial structures in Figs. 8a and 8c are similar

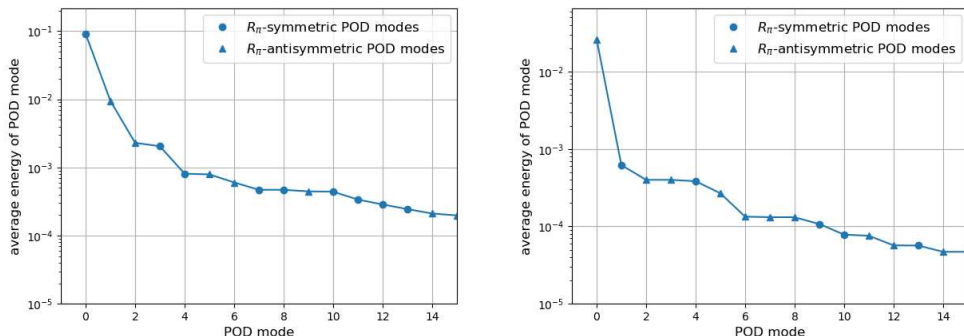


Fig. 5. POD spectra (average energies in the time window studied) in the saturated phase at $\text{Re} = 1500$, $\text{Rm} = 150$, $\mu_r = 50$. (a) POD spectrum of \mathbf{u} . (b) POD spectrum of \mathbf{H} .

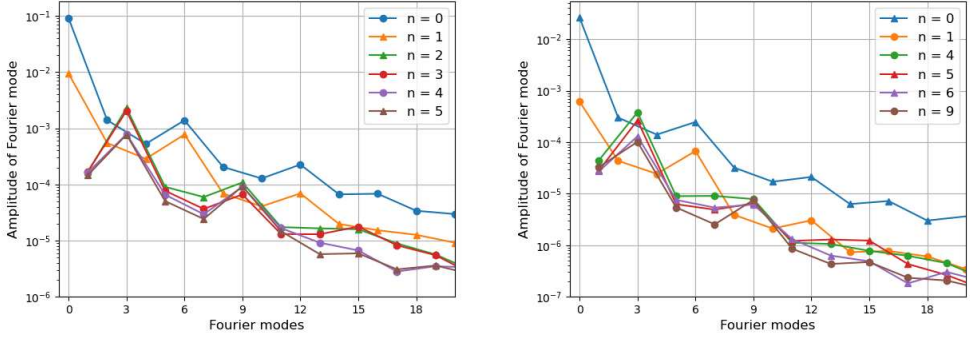


Fig. 6. Fourier spectra of the main POD modes in the saturated phase at $\text{Re} = 1500$, $\text{Rm} = 150$, $\mu_r = 50$. Note that the spectra have either odd or even Fourier modes but never couple the two. Modes with circles (resp. triangles) are R_π -symmetric (resp. R_π -antisymmetric). (a) POD modes of \mathbf{u} . (b) POD modes of \mathbf{H} .

to those from Figs. 4a and 4c in the growth phase. Next ϕ_1 (8.16% of \mathbf{u} 's energy) and ψ_1 (2.05% of \mathbf{H} 's energy) have opposite symmetry in comparison, respectively, with ϕ_0 and ψ_0 (Fig. 5) and are dominated again by their axisymmetric components (Fig. 6). Contrary to the symmetry-breaking components ϕ_5 and $\psi_{N,7}$ from the growth phase, these POD modes, which have gained a lot of importance since the growth phase, have time-amplitudes which are oscillating around non-zero values (Fig. 7). As a result, the mean fields of both \mathbf{u} and \mathbf{H} do not display pure symmetries as in the growth phase. Also Figs. 8b and 8d show, respectively, one cell and two cells for \mathbf{u} and \mathbf{H} , the two being interpreted as a dipole and a quadrupole. We note that the quadrupole in \mathbf{H} is geometrically similar to the one sketched for instance in [21, 22]. They differ from Fig. 4, which shows how the feedback of \mathbf{H} on \mathbf{u} changes the flow pattern. Regarding \mathbf{u} , the addition of a quadrupole and an axial dipole can be interpreted as a vertical shift of the shear layer which is not located at $z = 0$ anymore: the R_π -symmetry of the mean flow is broken even though there is, on average, no injection of angular momentum in the exactly counter-rotating configuration. To visualize this, we summed the space-contributions of ϕ_0 and ϕ_1 at the fixed time $t = 200$ from Fig. 7a and plotted streamlines colored by

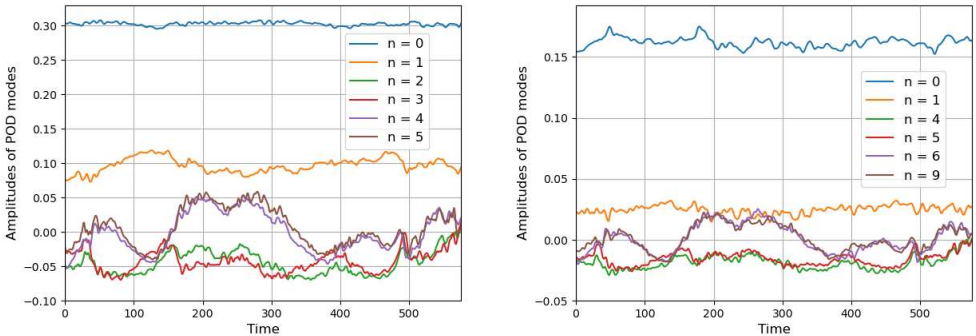


Fig. 7. Time evolution of the main POD modes in the saturated phase (only the time window without data-augmentation is displayed). (a) Time evolution of the main POD modes of \mathbf{u} . (b) Time evolution of the main POD modes of \mathbf{H} .

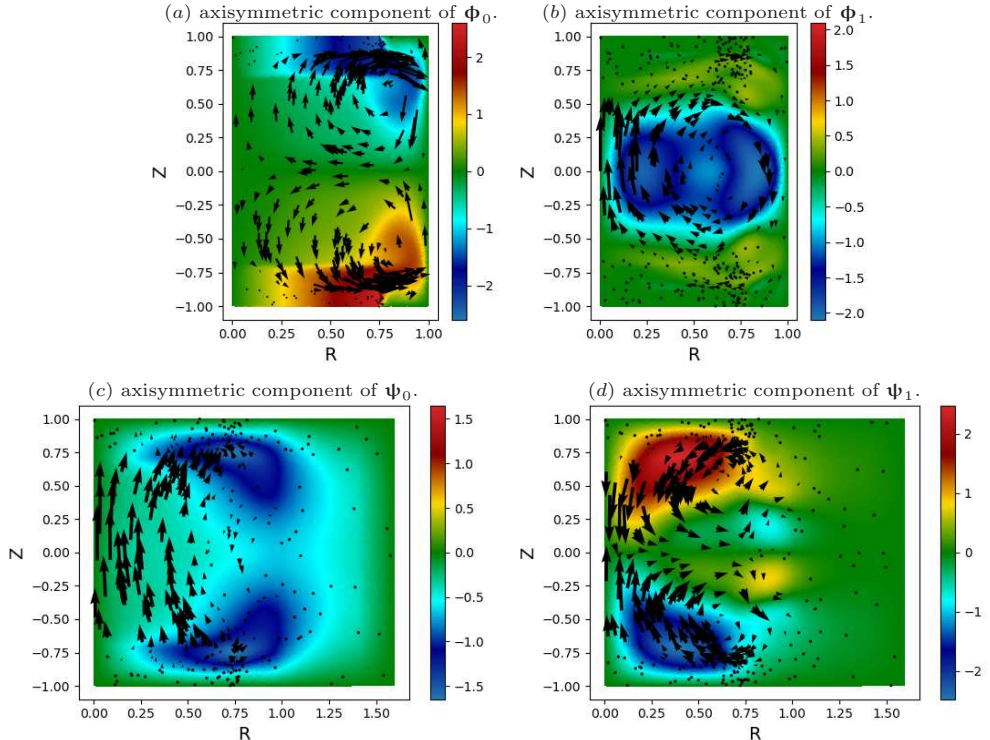


Fig. 8. 2D representation of the main axisymmetric POD modes in the saturated phase. Panels (a) and (b) (resp. (c) and (d)) have opposite symmetries and are the mean axisymmetric components of \mathbf{u} (resp. \mathbf{H}_N). In the time window studied, Φ_1 and Ψ_1 have time-amplitudes which do not average to zero.

the z -amplitude in Fig. 9a. While we do recognize the two cells with opposite azimuthal components, it is clear that the shear layer's position is displaced towards the negative z . This shift has a different impact on \mathbf{H} . Indeed, the relative energy of the symmetry-breaking component of \mathbf{u} with respect to its mean-field is 1/10, while it is 1/40 in the case of \mathbf{H} . As a result, the quadrupole in \mathbf{H} is not strong enough to create a visible shear layer, i.e. to create a region, where both vertical contributions cancel out. But plotting streamlines as for \mathbf{u} , we can see in Fig. 9b that the maximum vertical magnetic field is not localized at $z = 0$ but is slightly shifted towards the negative z , as expected when summing the two contributions from Figs. 8c and 8d with positive time-amplitudes (at $t = 200$ in Fig. 7b). This shift is also in agreement with the experimental observations reported in [18].

Continuing the POD analysis, we see that both \mathbf{u} and \mathbf{H} display four highly-energetic POD modes dominated by their $m_F = 3$ mode (Fig. 6): Φ_2, Φ_3, Φ_4 and Φ_5 accounting for 5.11% of the \mathbf{u} 's energy, and Ψ_4, Ψ_5, Ψ_6 and Ψ_9 accounting for 2.95% of the \mathbf{H} 's energy. Indeed, regarding the velocity field, since the Kelvin–Helmholtz rolls are produced by the strong velocity gradients from the shear layer, they should also be vertically shifted. Heuristically, combining two POD modes in the growth phase leads to a degree of freedom in θ . Multiplying again by 2 the number of POD modes adds another degree of freedom, this time in z . Then, assuming that the mechanism producing the $m_F = 3$ modes in \mathbf{H} is similar to the one studied in the growth phase, the α -effect is stronger

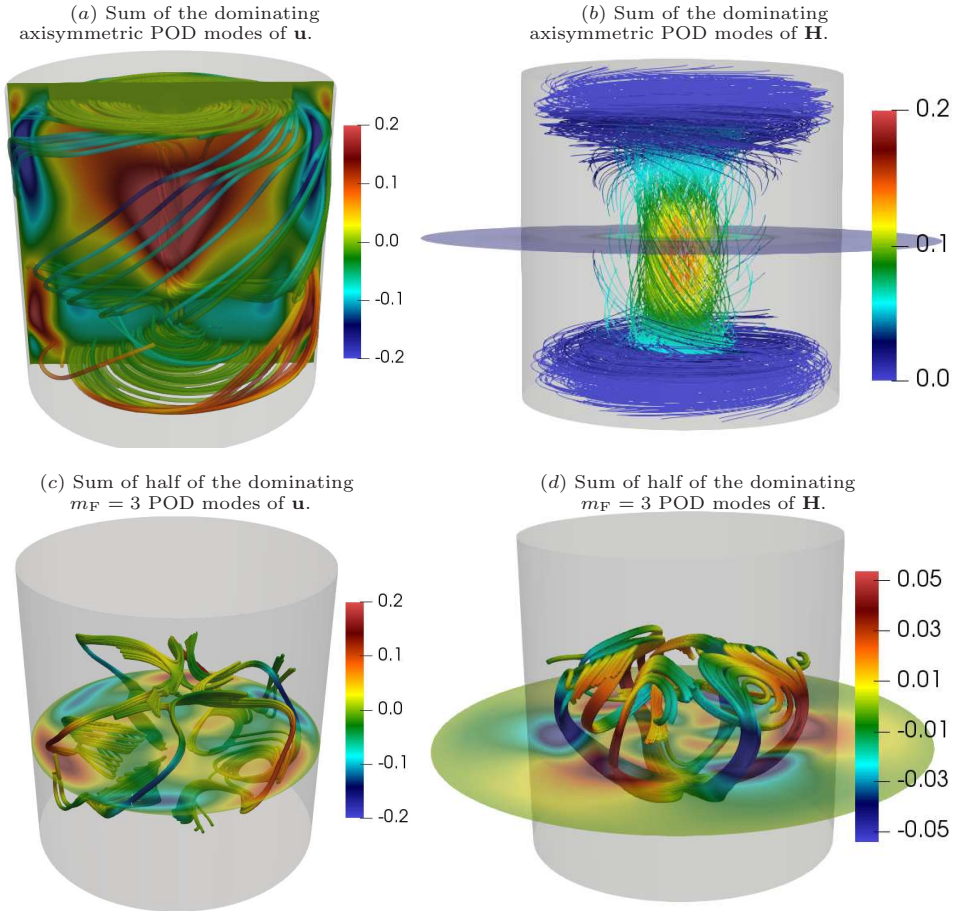


Fig. 9. Streamlines representation of the dominating POD modes of \mathbf{u} and \mathbf{H} in the saturated phase. The grey cylinder delimits the domain in which the fluid is free to move. The planes have equations (a) $y = 0$, (b) $z = 0$, (c) $z = -0.25$ and (d) $z = -0.3$. Planes of (c) and (d) are taken approximately at the \mathbf{u} shear layer altitude. POD modes are summed with their respective time-amplitudes at $t = 200$. Note that the quadrupole in \mathbf{H} is too weak to actually produce a shear layer in \mathbf{H} , but that it does displace the maximum of H_z . Lines are colored by their z -component.

close to the shear layer, therefore, shifting vertically the Kelvin–Helmholtz rolls in \mathbf{H} in the same manner as for \mathbf{u} . Looking at Fig. 7, we notice that the time-amplitudes can gather two by two the POD modes of both fields. For instance, up to some fluctuations, we can consider the sum of modes ψ_4 and ψ_5 on the one hand, and ψ_6 and ψ_9 on the other hand, instead of considering the four modes individually. The reason why POD calculations give them separately is their opposite R_π -symmetry highlighting again the spontaneous breaking of this symmetry. Therefore, to visualize streamlines, it makes sense to plot $\phi_4 + \phi_5$. Doing the same for $\phi_2 + \phi_3$ gives similar results since, in practice, $(\phi_2 + \phi_3)$ and $(\phi_4 + \phi_5)$ show common features characteristic of a rotation in θ [15]. Following this, we plot streamlines of the sum of ϕ_4 with ϕ_5 at $t = 200$ in Fig. 9c and the sum of ψ_6 with ψ_9 in Fig. 9d at $t = 200$. As expected it results that the

structures are not centered on $z = 0$ but rather shifted towards negative z .

If we reason about \mathbf{u} , the same being doable about \mathbf{H} , assuming perfect equalities between $a_2 = a_3$ and $a_4 = a_5$, the sum of all four POD modes gives rise to a physical field whose only degrees of freedom are the angle θ and its magnitude such as for the $m_F = 3$ components in [15]. Subtracting fluctuations $a_2 - a_3 = \gamma(t)$ gives the possibility of a variation in position along z as well as a modulation in the field structures which are left for future study.

Eventually the velocity and magnetic fields show POD modes dominated by azimuthal Fourier modes multiple of 8 (located inside the blades): the POD modes Φ_6 , Φ_7 , Ψ_2 and Ψ_3 are dominated by their $m_F = 8$ components and Ψ_7 and Ψ_8 are dominated by their $m_F = 16$ components (not shown), the interpretations remaining the same as in the growth phase. These modes account for 0.92% of the \mathbf{u} 's energy and 3.5% of the \mathbf{H} 's energy.

In summary the first eight modes of \mathbf{u} and ten modes of \mathbf{H} account for, respectively, 92.7% of \mathbf{u} 's energy and 95.2% of \mathbf{H} 's energy. Comparing with the values found in the growth phase, we note that, in a sense, saturation of magnetic energy weakens all fluctuations that most of the energy is captured by a small number of POD modes, suggesting that it may be possible to obtain correct descriptions of these fields with few degrees of freedom.

5. Conclusion and discussion.

In this study, we applied POD on the symmetric VKS setup with soft-iron impellers to understand its large-scale structures. We studied the growth and the saturated phases of the dynamo regime at $(\text{Re}, \text{Rm}) = (1500, 150)$. In the growth phase we were able to understand the variations of the dominant eigenmode and how \mathbf{u} transfers its $m_F = 3$ structures to \mathbf{H} . Our study in the saturated regime shows that the magnetic field's feedback on the velocity field has a profound impact on the system's structure though the most energetic POD modes remain roughly unchanged. The main result, which was unexpected in the exactly counter-rotating configuration, is that the velocity's shear layer is displaced vertically from $z = 0$. The mean magnetic field is modified in the sense that it is no longer strictly R_π -antisymmetric on the average. It is very well described by a decomposition into a dipole Ψ_0 , the same as the one growing in the growth phase, and a quadrupole Ψ_1 , which cannot be compared to any POD mode from the growth phase. Meanwhile, the velocity field still manages to pass its Kelvin-Helmholtz roll-structure to the magnetic field, and these structures are now described by four distinct POD modes, which is a sign of a vertical shift coordinated with that of the shear layer, as expected. Future work should aim to understand the origin of this vertical shift given that there is no injection of angular momentum. It would be also interesting to confirm this behavior for higher Re especially in the saturated phase since it is known that the velocity field's structure does not change too much [15], which, in turn, should not affect the growth phase.

If this is indeed the case, it would have important implications regarding the several regimes that were experimentally characterized by asymmetric forcing with different impeller frequencies $F_{\text{lower}} \neq F_{\text{upper}}$ [22]. It would also mean that, as briefly mentioned in [23], the path that is taken to certain parameters $(F_{\text{lower}}, F_{\text{upper}})$ is crucial. Indeed, here we studied the (F, F) system and it is likely that if we rerun it from $(F+f, F)$ or $(F, F+f)$, we would obtain two different results. Although the two systems are theoretically symmetrical with respect to each other, we would probably obtain a displacement of the shear layer towards $z = 0$ in the first case and towards the lower impeller in the

second case, which would, therefore, leads to potentially four equilibrium positions from which we could obtain two physically different situations that open the way to hysteresis or bistability. An interesting tool to achieve this behavior would be POD Galerkin [19]. Indeed, the decomposition of a magnetic field into a dipole and a quadrupole is often used when building low-dimensional systems [24, 25], which is a sign that POD Galerkin might be efficient in this situation. But to do this, it will be necessary to take into account the variation in space and time of μ_r , which is known to be fundamental to understanding energy transfers [10].

Acknowledgements. This work was performed using HPC resources from GENCI-TGCC (Grant 2024-0254).

References

- [1] A. GAILITIS, *et al.* Colloquium: Laboratory experiments on hydromagnetic dynamos. *Reviews of Modern Physics*, vol. 74 (2002), no. 4, p. 973.
- [2] R. STIEGLITZ AND U. MÜLLER. Experimental demonstration of a homogeneous two-scale dynamo. *Physics of Fluids*, vol. 13 (2001), no. 3, pp. 561–564.
- [3] J.-L. GUERMOND, *et al.* Effects of discontinuous magnetic permeability on magnetodynamic problems. *Journal of Computational Physics*, vol. 230 (2011), no. 16, pp. 6299–6319.
- [4] R. MONCHAUX, *et al.* Generation of a magnetic field by dynamo action in a turbulent flow of liquid sodium. *Phys. Rev. Lett.*, vol. 98 (2007), p. 044502.
- [5] S. MIRALLES, *et al.* Dynamo threshold detection in the von Kármán sodium experiment. *Phys. Rev. E*, vol. 88 (2013), p. 013002.
- [6] R. PASQUETTI, R. BWEMBA, AND L. COUSIN. A pseudo-penalization method for high Reynolds number unsteady flows. *Applied Numerical Mathematics*, vol. 58 (2008), no. 7, pp. 946–954.
- [7] A. GIESECKE, F. STEFANI, AND G. GERBETH. Role of soft-iron impellers on the mode selection in the von Kármán–sodium dynamo experiment. *Phys. Rev. Lett.*, vol. 104 (2010), p. 044503.
- [8] A. GIESECKE, *et al.* Electromagnetic induction in non-uniform domains. *Geophysical and Astrophysical Fluid Dynamics*, vol. 104 (2010), no. 5–6, pp. 505–529.
- [9] C. NORE, D.C. QUIROZ, L. CAPPANERA, AND J.-L. GUERMOND. Numerical simulation of the von Kármán sodium dynamo experiment. *Journal of Fluid Mechanics*, vol. 854 (2018), pp. 164–195.
- [10] M. CREFF, *et al.* Tracking dynamo mechanisms from local energy transfers: Application to the von Kármán sodium dynamo. *Phys. Plasmas*, vol. 31 (2024), no. 2, p. 022306.
- [11] G. BERKOOZ, P. HOLMES, AND J.L. LUMLEY. The proper orthogonal decomposition in the analysis of turbulent flows. *Annual Review of Fluid Mechanics*, vol. 25 (1993), no. 1, pp. 539–575.

- [12] L. SIROVICH. Turbulence and the dynamics of coherent structures part I: Coherent structures. *Quarterly of Applied Mathematics*, vol. 45 (1987), no. 3, pp. 561–571.
- [13] P. HOLMES, J.L. LUMLEY, AND G. BERKOOZ. *Turbulence, Coherent Structures, Dynamical Systems and Symmetry*. Cambridge Monographs on Mechanics (Cambridge University Press, 1996).
- [14] C. NORE, L. TUCKERMAN, O. DAUBE, AND S. XIN. The 1:2 mode interaction in exactly counter-rotating von Kármán swirling flow. *Journal of Fluid Mechanics*, vol. 477 (2003), pp. 51–88.
- [15] R. BOUSQUET, *et al.* Large scale analysis of three-dimensional turbulent von Kármán swirling flows. *Physics of Fluids*, vol. 36 (2024), no. 10, p. 105133.
- [16] F. RAVELET, A. CHIFFAUDEL, AND F. DAVIAUD. Supercritical transition to turbulence in an inertially driven von Kármán closed flow. *Journal of Fluid Mechanics*, vol. 601 (2008), p. 339364.
- [17] P.-P. CORTET, A. CHIFFAUDEL, F. DAVIAUD, AND B. DUBRULLE. Experimental evidence of a phase transition in a closed turbulent flow. *Phys. Rev. Lett.*, vol. 105 (2010), p. 214501.
- [18] J. BOISSON, *et al.* Symmetry and couplings in stationary von Kármán sodium dynamos. *New Journal of Physics*, vol. 14 (2012), no. 1, p. 013044.
- [19] B. PODVIN, *et al.* Proper orthogonal decomposition analysis and modelling of the wake deviation behind a squareback Ahmed body. *Phys. Rev. Fluids*, vol. 5 (2020), p. 064612.
- [20] R. LAGUERRE, *et al.* Impact of impellers on the axisymmetric magnetic mode in the VKS2 dynamo experiment. *Phys. Rev. Lett.*, vol. 101 (2008), p. 104501.
- [21] S. AUMATRE, *et al.* The VKS experiment: turbulent dynamical dynamos. *Comptes Rendus Physique*, vol. 9 (2008), no. 7, pp. 689–701.
- [22] F. RAVELET, *et al.* Chaotic dynamos generated by a turbulent flow of liquid sodium. *Phys. Rev. Lett.*, vol. 101 (2008), p. 074502.
- [23] R. MONCHAUX, *et al.* The von Kármán sodium experiment: Turbulent dynamical dynamos. *Physics of Fluids*, vol. 21 (2009), no. 3, p. 035108.
- [24] F. PÉTRÉLIS AND S. FAUVE. Chaotic dynamics of the magnetic field generated by dynamo action in a turbulent flow. *Journal of Physics: Condensed Matter*, vol. 20 (2008), no. 49, p. 494203.
- [25] C. GISSINGER. A new deterministic model for chaotic reversals. *The European Physical Journal B*, vol. 85 (2012), p. 137.

Received 24.11.2024